OxLDL-targeted iron oxide nanoparticles for in vivo MRI detection of perivascular carotid collar induced atherosclerotic lesions in ApoE-deficient mice

Song Wen (文颂),* Dong-Fang Liu (柳东芳) ,* Zhen Liu (刘振),† Steven Harris,§ Yu-Yu Yao (姚玉宇), Qi Ding (丁琪),†† Fang Nie (聂芳),* Tong Lu (卢瞳) ,* Hua-Jun Chen (陈华俊),* Yan-Li An (安艳丽),* Feng-Chao Zang (臧凤超),* and Gao-Jun Teng (滕皋军)[1],***

Jiangsu Key Laboratory of Molecular and Functional Imaging,* Department of Radiology, Zhongda Hospital, Medical School, Southeast University, Nanjing, China; Atherosclerosis Research Center,† Nanjing Medical University, Nanjing, China; Department of Biomedical Engineering,§ Emory University/Georgia Institute of Technology, Atlanta, GA; Department of Cardiology,** Zhongda Hospital, Southeast University, Nanjing, China; and Jiangsu Key Laboratory for Biomaterials and Devices,†† State Key Laboratory of Bioelectronics, School of Biological Science and Medical Engineering, Southeast University, Nanjing, China

Abstract Atherosclerotic disease is a leading cause of morbidity and mortality in developed countries, and oxidized LDL (OxLDL) plays a key role in the formation, rupture, and subsequent thrombus formation in atherosclerotic plaques. In the current study, anti-mouse OxLDL polyclonal antibody and nonspecific IgG antibody were conjugated to polyethylene glycol-coated ultrasmall superparamagnetic iron oxide (USPIO) nanoparticles, and a carotid perivascular collar model in apolipoprotein E-deficient mice was imaged at 7.0 Tesla MRI before contrast administration and at 8 h and 24 h after injection of 30 mg Fe/kg. The results showed MRI signal loss in the carotid atherosclerotic lesions after administration of targeted anti-OxLDL-USPIO at 8 h and 24 h, which is consistent with the presence of the nanoparticles in the lesions. Immunohistochemistry confirmed the colocalization of the OxLDL/macrophages and iron oxide nanoparticles. The nonspecific IgG-USPIO, unconjugated USPIO nanoparticles, and competitive inhibition groups had limited signal changes ($p < 0.05$). This report shows that anti-OxLDL-USPIO nanoparticles can be used to directly detect OxLDL and image atherosclerotic lesions within 24 h of nanoparticle administration and suggests a strategy for the therapeutic evaluation of atherosclerotic plaques in vivo.—Wen, S., D-F. Liu, Z. Liu, S. Harris, Y-Y. Yao, Q. Ding, F. Nie, T. Lu, H-J. Chen, Y-L. An, F-C. Zang, and G-J. Teng. **OxLDL-targeted iron oxide nanoparticles for in vivo MRI detection of perivascular carotid collar induced atherosclerotic lesions in ApoE-deficient mice. *J. Lipid Res.* 2012.** 53: **829–838.**

Supplementary key words atherosclerosis • molecular imaging • magnetic resonance imaging • low density lipoprotein

Despite significant diagnostic and therapeutic advances achieved in the last few decades, atherosclerotic disease is still a leading factor contributing to morbidity and mortality worldwide (1). Vulnerable plaques with large lipid cores, thin fibrous caps, and increased inflammatory cell infiltrate may be more prone to rupture, exposing the thrombogenic material of the plaque core, precipitating acute coronary syndrome, and myocardial infarction (2). It is necessary to develop diagnostic tools that can characterize plaque composition, especially components that mediate the transition of stable plaques to vulnerable plaques (3).

Oxidized LDL (OxLDL) plays a key role in atherosclerotic plaque formation, rupture, and thrombotic ischemia in animal models and humans (4). OxLDL stimulates the transformation of macrophages and vascular smooth muscle cells into lipid-rich foam cells, induces the proliferation and migration of vascular cells, and retards endothelial regeneration (5). Recent human studies have shown that vulnerable plaques are enriched in OxLDL and that increased circulating levels of OxLDL are associated with acute coronary syndrome and plaque disruption (6). Furthermore, removal of circulating OxLDL has proven to be a promising strategy for the treatment of atherosclerosis (7). Therefore, the development of sensitive molecular imaging probes directly targeting OxLDL in the vessel wall may allow for in vivo characterization of plaque vulnerability.

This work was supported by National Natural Science Foundation of China (NSFC #30910103905, #81101139, #81070085).

✤***Author's Choice**—Final version full access.*

Manuscript received 23 July 2011 and in revised form 29 February 2012.

Published, JLR Papers in Press, March 5, 2012
DOI 10.1194/jlr.M018895

Abbreviations: apoE$^{-/-}$, apolipoprotein E deficient; DLS, dynamic light scattering; OSE, oxidation-specific epitope; OxLDL, oxidized low-density lipoprotein; PEG, pegylated; rSI, relative signal intensity; USPIO, ultrasmall iron oxide particle.

[1] To whom correspondence should be addressed.
e-mail: gjteng@vip.sina.com

Briley-Saebo et al. (8–11) have recently demonstrated in vivo imaging of OxLDL by targeting oxidation-specific epitopes (OSEs), which are abundant in aortic atherosclerotic lesions of apolipoprotein E-deficient (apoE$^{-/-}$) mice, using MDA2, E06, and IK17 Fab. However, these antibodies are only targeted to a single oxLDL epitope (12, 13). Moreover, the aortic atherosclerotic lesions induced by long periods of fat-feeding used in these studies were stable and did not lead to plaque rupture (14, 15), unlike a carotid perivascular collar model in apoE$^{-/-}$ mice in the presence of hypercholesterolemia that offers reproducible site-controlled neointimal formation and stenosis, which is more likely to reflect the complex pathogenesis seen in clinical practice (16, 17).

MRI has emerged as a leading noninvasive imaging modality for assessing plaque burden and evaluating plaque composition with extraordinarily high temporal and spatial resolution (18, 19). However, MR imaging with endogenous contrast is not sufficient for plaque characterization (20), and contrast agents are needed improve the detection and characterization of vulnerable plaques. Ultrasmall superparamagnetic iron oxide (USPIO) nanoparticles are MRI contrast agents that produce large local magnetic susceptibilities that lead to signal loss in T2 or T2* weighted images. These nanoparticles have been extensively studied and applied to imaging atherosclerosis (8, 21), cancer (22), and targeted-drug therapy (23), and they can be safe for human administration (21, 24).

In previous investigations, Gao and colleagues (25–28) established a synthetic route for achieving water-soluble and biocompatible polyethylene glycol (PEG)-coated Fe_3O_4 nanocrystals, which were prepared via a "one-pot" route. MRI studies have demonstrated that these nanoparticles are useful in tumor detection via passive (25) or active targeting in vivo (26, 27).

In this study, PEG-coated USPIO nanoparticles with polyclonal rabbit anti-copper-oxide mouse LDL antibody were developed to generate a novel, targeted MRI contrast agent. These nanoparticles were used to detect plaques in an in vivo perivascular collar-induced atherosclerotic lesion model in carotid arteries of apoE$^{-/-}$ mice. The results show that the anti-OxLDL-USPIO nanoparticles has excellent diagnostic ability as an MRI contrast agent, suggesting further potential for characterizing carotid atherosclerotic lesions.

MATERIALS AND METHODS

Materials

PEG-coated USPIO nanoparticles (Fe_3O_4 nanocrystals, mean size 11.8 ± 0.5 nm, using α,ω-dicarboxyl-terminated PEG [HOOC-PEG-COOH, Mn = 2000] as the surface capping agent) (25) and synthesized using the "one-pot" reaction were kindly provided by the Laboratory of Colloid, Interface and Chemical Thermodynamics, Institute of Chemistry, Chinese Academy of Sciences, Beijing, China. Polyclonal rabbit anti-copper-oxide mouse LDL antibody (IgG, MW 150 KD, >99% pure) was purchased from Biosynthesis Biotechnogy Co. (Beijing, China). 1-Ethyl-3-(dimethylaminopropyl) carbodiimide hydrochloride (EDC.HCl) and Sulfo-N-hydrosuccinimide (Sulfo-NHS) were purchased from Medpep Co. (Shanghai, China).

Synthesis of OxLDL targeted USPIO nanoparticles

To prepare the OxLDL-targeted USPIO nanoparticles, 1 mg of PEG-coated USPIO nanoparticles was diluted in 200 μl boric acid/borate buffer (pH 9, 0.2 M). EDC.HCl (1 mg) and Sulfo-NHS (0.5 mg) was then added to the particle solution (EDC.HCl and Sulfo-NHS dissolve in borate buffer) and mixed well. The reaction continued for 30 min with continuous mixing. Then 200 μg anti-mouse OxLDL antibody (dissolved in 100 μl PBS, 0.1 M, pH 7.4) was added, and the mixture was stirred for 3 h at room temperature. Then, conjugated USPIO nanoparticles were purified three times with PBS using a centrifugal filter device and stored in PBS (0.1 M, pH 7.4) at 4°C (29). Normal mouse IgG conjugated USPIO and nonconjugated USPIO nanoparticles were used as controls.

Characterization of conjugated USPIO

The morphology of the USPIO nanoparticles was characterized by transmission electron microscopy (JEOL-100CX), and particle sizes and size distributions were calculated using at least 300 particles and image analysis software (Image-Pro Plus 5.0; Media Cybernetics). The hydrated particle sizes were characterized by dynamic light scattering (DLS) (90 Plus Particle Size Analyzer; Brookhaven Instruments), and the magnetic properties of the iron oxide nanoparticles were investigated using a vibrating sample magnetometer (Lakeshore 7407). The longitudinal (R1) and transverse (R2) relaxivities at 3.0 Tesla were measured in PBS at 25°C using a clinical MRI scanner (Philips Achieva 3.0 T; operating frequency 128 MHz). The longitudinal (R1) and transverse (R2) relaxation rates were determined at five different concentration levels (0.1–0.5 mmol/l Fe) using a Look Locker T1 mapping sequence (repetition time/echo time 3.8/1.9 ms, Flip angle 7°) and a Multi-Slice Multi-Echo T2 mapping sequence (repletion time 2500 ms, echo time 19–112 ms, 16 echoes, Flip angle 180°), respectively. All relaxivity values were calculated as the slope associated with a linear fit of the iron oxide concentration (mmol/l Fe) versus R1 (mmol/s) or R2 (mmol/s).

The specificity of the targeted nanoparticles binding to copper-oxide LDL was evaluated with a mouse OxLDL ELISA kit (Y-J Biological, Shanghai, China). Antibody content per USPIO nanoparticleswas estimated using a Braford protein assay kit (Keygentec, China) combined with the phenanthronline chemical iron quantification method (26). To assess the stability of the targeted and untargeted USPIO nanoparticles, the hydrodynamic size of the USPIO nanoparticles in PBS or 10% FBS was analyzed by DLS measurement within 24 h. The particles sized were measured for 4 weeks with storage in the dark at 4°C with ambient humidity.

Radioiodination of conjugated USPIO

Radiolabeling of anti-OxLDL-USPIO nanoparticles with ^{125}I was performed by the chloramine-T method (30). The iodinated anti-OxLDL-USPIO nanoparticles were separated from excess reactants by passage through a Sephadex G-25 column. Anti-OxLDL-USPIO nanoparticles were labeled with ^{125}I to specific activities of 10 μCi μg^{-1} protein. As control, normal mouse IgG-USPIO nanoparticles were labeled with ^{125}I by a similar method.

Pharmacokinetic and biodistribution of conjugated USPIO nanoparticles

apoE$^{-/-}$ mice (6–8 weeks old) on a C57BL/6 background receiving a western-type diet (10% grease, 2% cholesterol, and 0.5% cholate; Cooperative Medical Biological Engineering Co.,

Nanjing, China) ad libitum beginning at 8 weeks until 28 to 32 weeks of age were used for all studies. Age-matched C57BL/6 wild-type (WT) mice on normal chow until 28 to 32 weeks of age were used as control subjects. The biodistribution of ^{125}I-labeled anti-OxLDL-USPIO and ^{125}I-labeled normal mouse IgG-USPIO nanoparticles was examined in apoE$^{-/-}$ mice and C57BL/6 WT mice (8, 10). Five apoE$^{-/-}$ mice and five WT mice in one group were administered 30 μCi of ^{125}I-labeled anti-OxLDL-USPIO via intravenous tail vein injection, and another group (five apoE$^{-/-}$ mice and five WT mice) was injected with 30 μCi of ^{125}I-labeled normal mouse IgG-USPIO nanoparticles. Ten microliters of blood were collected from the tail vein at 5 min, 30 min, and 1, 2, 4, 8, and 24 h after injection. Blood pool activity was corrected for decay and normalized by dividing by the initial blood pool counts. The normalized blood pool data were analyzed by biexponential (two-compartment) curve fitting. Twenty-four hours after injection, tissues from the liver, lung, heart, spleen, stomach, colon, kidney, bone, and muscle were collected, and the radioactivity in each tissue was counted by a γ scintillation counter. The results are expressed as the percentage of the injected dose per g (%ID/g).

In vitro analysis of USPIO nanoparticle uptake

Murine macrophages (RAW 264.7) were obtained from the Shanghai Cell Bank (Type Culture Collection Committee, Chinese Academy of Science, China). Cells were cultured in DMEM media (Gibco, Carlsbad, CA) containing 10% FBS, 1% penicillin-streptomycin, 1% glutamine, and 1% sodium pyruvate in an incubator with 5% CO_2 at 100% humidity and 37°C. Cells between passages 4 and 6 were used in the experiments.

Similar to the studies by Briley-Saebo et al. (8, 10), in vitro cell studies were performed to determine the extent of passive uptake of PEG-coated targeted and untargeted USPIO nanoparticles in quiescent and activated foaming macrophages. USPIO nanoparticles were incubated with cultured macrophages under four conditions: preincubation of macrophages with or without mouse OxLDL and preincubation of USPIO nanoparticles with or without mouse OxLDL (8). To perform these experiments, 1×10^6 RAW264.7 macrophages were plated in 12-well plates with DMEM containing 10% FBS. In one set of wells, mouse OxLDL (100 μg/ml) was added and incubated with macrophages for 12 h at 37°C, and in the other no OxLDL was added. The macrophages were exposed to similar conditions. The wells were washed three times with fresh DMEM, and the macrophages were used in the following experiments. In a similar manner, anti-OxLDL-USPIO (n = 3), normal mouse IgG-USPIO (n = 3), and unconjugated USPIO nanoparticles (n = 3) were preexposed or not to mouse OxLDL (100 μg/ml) for 2 h at 37°C. The USPIO nanoparticles were then incubated with the macrophages for an additional 12 h at 37°C. Resovist (Ferucarbotran, Schering, Germany), a commercially available and passively macrophage-targeted SPIO, was used as a control nanoparticle. Internalized iron oxide particles were detected with Perl's staining with nuclear fast red counterstaining.

Animal protocol

All experimental animal protocols were approved by the animal care committee of Southeast University, Nanjing, China. Male apoE$^{-/-}$ mice on a C57BL/6 background (n = 20), aged 10–12 weeks, were acquired from the Department of Laboratory Animal Science, Peking University Health Science Center (Beijing, China). Mice were kept on a 12/12 h light-dark cycle with food and water freely available. The animals received a western-type diet for 2 weeks before surgery. All mice underwent surgery after deep anesthesia induced by subcutaneous injection of 60 mg/kg ketamine (Hengrui Medicine Co., LTD, Jiangsu, China) and 1.26 mg/kg fentanyl citrate (Yichang Humanwell Pharmaceutical Co., LTD, Sichuan, China). As described by von der Thusen (16), carotid atherosclerotic lesions were induced using bilateral perivascular polyethylene collars (PE0503; AniLab Software and Instruments Co., Ningbo, China). Collars (1.5–2 mm long and 0.25 mm internal diameter) were placed on the common carotid arteries with an average adventitial diameter of 0.5 mm. The axial edges were approximated by the placement of two or three circumferential silk ties. All procedures were performed under a stereomicroscope. The entry wounds were closed, and the animals were returned to their cages and remained on the western-type diet for 3 weeks. Two mice died after surgery. The 18 remaining apoE$^{-/-}$ mice were assigned to the following experimental groups: six anti-OxLDL-USPIO nanoparticles, four untargeted IgG-USPIO nanoparticles, four unconjugated USPIO nanoparticles, and four for the in vivo competitive inhibition study.

In vivo MRI

In vivo MRI was performed at 7.0 Tesla using a 35-mm birdcage coil and mouse cradle. Animals were initially anesthetized with a 4% isoflurane/air gas mixture delivered through a nose cone and maintained under anesthesia with a 1.5–2% isoflurane/air gas mixture. MRI was performed preceding nanoparticle administration and at 8 and 24 h after the tail vein injection of 30 mg Fe/kg body weight USPIO nanoparticles over 1 min. For in vivo competitive inhibition, age-matched apoE$^{-/-}$ mice (n = 4) received tail vein injection of a mixture of 1 mg free anti-OxLDL antibody and 30 mg/kg body weight anti-OxLDL-USPIO nanoparticles. The following MRI sequences were used (*1*): 3D Fast Low Angle Shot (FLASH): repetition time/echo time = 15 ms/2.5 ms, Flip angle = 20°, number of averages = 1; (*2*) T2-PD (proton density) weighted dual-echo Multi-Slice Multi-Echo: repetition time = 3,058.5 ms, echo time = 65/13 ms, slice thickness = 0.5 mm, slices = 25, number of averages = 3, matrix = 256 × 256. The total imaging time for each time point was less than 40 min.

Image quality and image analysis

Two experienced radiologists independently reviewed each MR study. Image quality was rated for each artery and contrast weighting on a five-point scale (with 1 being poor and 5 excellent) based on the overall signal-to-noise ratio of the image and the clarity of the vessel wall boundary. Slices with image quality less than 2 were excluded from the study. Preinjection images and MR images taken 8 h and 24 h after USPIO injection were manually coregistered according to plaque morphology and the distance from the upper edge of the aortic arch. Changes in the relative signal intensity (rSI) between the preinjection and the 8 h and 24 h postUSPIO images were measured within the entire noncalcified portion of athermanous plaque. Image measurements were made using Paravision 5.0 software by an independent reader who was blind to the histological analysis. The rSI was defined as the ratio of the signal intensity (SI) in the user-defined plaque area (SI_{plaque}) to the SI in the adjacent sternocleidomastoid muscle (SI_{muscle}) for each MR image (24, 31). The percent of normalized enhancement (%NENH) describes the percent change in the rSI ratios obtained before and after injection: $\%NENH = (rSI_{post} - rSI_{pre} / rSI_{pre}) \times 100\%$, where rSI_{post} is the rSI value obtained after injection and rSI_{pre} is the rSI value obtained before administration of the USPIO.

Tissue harvest and section

After all MR imaging, the mice were anesthetized by an overdose of intraperitoneally injected chloral hydrate and perfused

with 50–100 ml PBS through the left ventricle, followed by 4% paraformaldehyde under physiological pressure. The bilateral common carotid arteries and organs, including the liver, spleen, and kidneys, were excised and embedded in Tissue-Tek OCT compound (Sakura Finetek Japan Co., Tokyo), frozen, and sectioned (CM1950; Leica). For the carotid arteries, serial consecutive cryosections were cut with a 6 μm thickness every 100 μm along the specimen, and approximately 200 sections were obtained per vessel. For the organs, serial consecutive cryosections were cut with a 10 μm thickness every 500 μm, and approximately 10 sections per organ were obtained.

Histomorphometry and immunohistochemistry

Sections obtained from the carotid arteries and organs were stained with hematoxylin and eosin for morphometric analysis. Perl's staining was applied to identify the USPIO nanoparticles. Sections were stained with polyclonal anti-OxLDL antibody (1:100; Biosynthesis Biotechnogy Co., Beijing, China) and anti-CD68 antibody (1:100; Biolegend, San Diego, CA) for macrophage immunoreactivity using an ultrasensitive SP immunohistochemical kit (Zhongshan Goldenbridge Biotechnology Co., Beijing, China). Light hematoxylin counterstaining was used to visualize all nuclei in the tissue sections. Negative control was added with PBS. All images were reviewed under light microscope (Scope.A1; Zeiss, Germany) with an independent pathologist. Computer-assisted morphometry was performed with Image Pro Plus 5.0. A mean of 10 randomly selected fields were counted for each section.

Statistical analysis

Data are indicated as mean ± standard deviation. All multiple comparisons were made by one-way ANOVA followed by a Tukey post hoc test. All statistical tests were performed using SPSS for windows (Version 13.0; SPSS), and a value of $P < 0.05$ was considered statistically significant.

RESULTS

Characterization of USPIO nanoparticles

The physical and chemical properties of the nanoparticles are summarized in **Table 1**. The transmission electron microscopy images (**Fig. 1A**) show that the anti-OxLDL-USPIO nanoparticles are well dispersed in PBS solution. Although they have the same iron core size, the anti-OxLDL-USPIO and nonspecific IgG-USPIO nanoparticles have greater hydrated diameters than unconjugated USPIO (28.8 ± 2.32 nm and 27.2 ± 3.99 nm vs. 19.0 ± 2.67 nm) (Fig. 1B, D). The saturation magnetization values of anti-OxLDL-USPIO and unconjugated USPIO are 53.1 and 52.4 emu/g Fe at 25°C, respectively (Fig. 1C). The R2 and R1 relaxivity values of anti-OxLDL-USPIO, untargeted IgG-USPIO, and unconjugated USPIO nanoparticles were 184.82 ± 5.27, 182.65 ± 5.76, and 192.12 ± 5.9 and 4.15 ± 0.11, 4.38 ± 0.02, and 4.26 ± 0.07, respectively. To assess the stability of the targeted and untargeted USPIO nanoparticles, the hydrodynamic size of the USPIO nanoparticles in PBS or 10% FBS was analyzed by DLS measurement. The hydrodynamic sizes did not change significantly within 24 h (Fig. 1D). In addition, the targeted anti-OxLDL-USPIO and untargeted IgG-USPIO nanoparticles exhibited limited (<10%) variation in hydrodynamic size after 4 weeks of storage in PBS at 4°C, showing excellent stability in an aqueous medium. The concentration of antibody per USPIO was 58.12 μg protein/mg Fe, and ELISA showed that the anti-OxLDL-antibody conjugated with USPIO nanoparticles retained its biological activity, whereas the unconjugated USPIO and boiled anti-OxLDL-USPIO nanoparticles had a negligible effect on the OD_{450} value (Fig. 1E).

In WT mice, the blood half-life was ~10.5 h for targeted or untargeted IgG-USPIO nanoparticles, consistent with the literature (32, 33). However, in apoE$^{-/-}$ mice, the targeted anti-OxLDL-USPIO maintained a longer half-life than the untargeted IgG-USPIO (14.13 h vs. 10.43 h). In addition, there was no significant difference in the percentage injected dose (%ID/g) in the liver and spleen between apoE$^{-/-}$ mice and WT mice for targeted USPIO or untargeted IgG-USPIO nanoparticles 24 h after ^{125}I-labeled anti-OxLDL-USPIO or ^{125}I-labeled IgG-USPIO injection (Table 1).

In vitro studies

Figure 2 summarizes the in vitro macrophage experiments assessing the association and uptake of the four types of USPIO nanoparticles by RAW264.7 macrophages under four conditions. Perl's staining showed that the highest uptake of iron oxide nanoparticles was when both the macrophages and anti-OxLDL-USPIO nanoparticles were

TABLE 1. Physical and chemical properties of nanoparticles

Formulation	Anti-OxLDL-USPIO	Untargeted IgG-USPIO	Unconjugated USPIO
Size (hydrodynamic diameter, nm)	28.2 ± 2.82	27.2 ± 3.99	19.0 ± 2.67
R1 at 128 MHz (s mmol/L)	4.15 ± 0.11	4.38 ± 0.02	4.26 ± 0.07
R2 at 128 MHz (s mmol/L)	184.82 ± 5.27	182.65 ± 5.76	192.12 ± 5.9
R2/R1 value	44.53	41.7	45.1
Blood half-life ApoE$^{-/-}$ (h)	14.13*	10.43	—
Blood half-life WT (h)	10.38	10.62	—
% ID/g in liver ApoE$^{-/-}$ (24 h p.i.)	4.24 ± 1.73	4.12 ± 0.79	—
% ID/g in liver WT (24 h p.i.)	5.62 ± 1.13	4.24 ± 1.56	—
% ID/g in spleen ApoE$^{-/-}$ (24 h p.i.)	4.17 ± 1.57	4.31 ± 0.70	—
% ID/g in spleen WT (24 h p.i.)	5.21 ± 1.08	4.41 ± 1.59	—

All values expressed as mean ± SD. All sizes are based upon the weighted averages. Relaxivities shown were obtained in PBS at 128 MHz and 25°C. All blood half-lives and percentage injected (p.i.) doses (%ID/g) in the liver and spleen were obtained in apoE$^{-/-}$ or WT mice after injection of 30 μCi ^{125}I-labeled nanoparticles. *$P < 0.05$ apoE$^{-/-}$ vs. WT mice. oxLDL, oxidized low-density lipoprotein; R1, longitudinal relaxation rate; R2, transverse relaxation rate; USPIO, ultrasmall iron oxide particle.

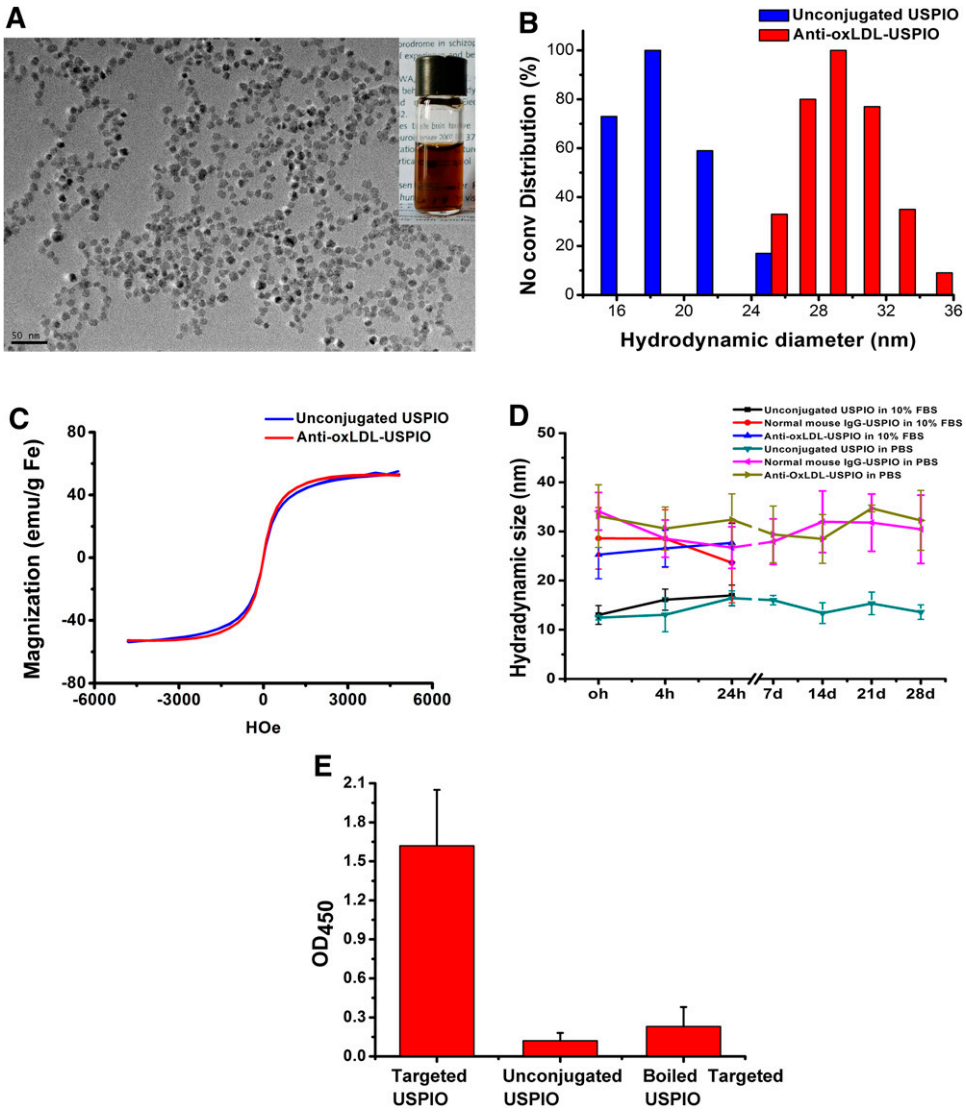

Fig. 1. Characterization of iron oxide nanoparticles. A: Representative TEM image of anti-OxLDL-USPIO nanoparticles. Upper insert shows a photograph of anti-OxLDL-USPIO solution in PBS. B: The dynamic light scattering diameters and (C) room-temperature magnetization curve of anti-OxLDL-USPIO and unconjugated USPIO nanoparticles. D: The stability curves of various USPIO nanoparticles in 10% FBS or PBS by DLS measurement. ELISA results show the biological activity of anti-OxLDL-USPIO nanoparticles, while boiled anti-OxLDL-USPIO and unconjugated USPIO have limited nonspecific adsorption on OD_{450} value (E). Data presented as mean ± SD (n = 3).

preexposed to OxLDL (Fig. 2D). On the other hand, when macrophages were preexposed to OxLDL but the anti-OxLDL-USPIO nanoparticles were not (Fig. 2B) or when the anti-OxLDL-USPIO nanoparticles was preexposed to OxLDL but the macrophages were not (Fig. 2C), the uptake of iron oxide nanoparticles was very limited. Cells incubated with untargeted IgG-USPIO (Fig. 2E–H) and unconjugated-USPIO nanoparticles (Fig. 2I, L) showed much less USPIO staining under all conditions. The results suggest that the PEG-coated USPIO nanoparticles significantly inhibited the nonspecific uptake of nanoparticles by RAW264.7 macrophages. However, because anti-OxLDL-USPIO nanoparticles may bind free mouse OxLDL in DMEM, they could be taken up as OxLDL/anti-OxLDL-USPIO complexes by activated foaming macrophages (induced by preexposing to OxLDL for 12 h, Oil O staining proved; data not shown). As anticipated, Resovist showed a large macrophage uptake (Fig. 2M).

In vivo MRI studies

Next, we administered 30 mg iron/kg body of the prepared iron oxide nanoparticles to apoE$^{-/-}$ mice with perivascular collar induced carotid atherosclerosis. **Fig. 3** shows representative in vivo MR images of the atherosclerotic carotid lesions obtained before and 8 h and 24 h after the injection of the different USPIO formulations. Fig. 3A–C shows that significant signal loss is observed at 8 h and 24 h after the administration of targeted anti-OxLDL-USPIO nanoparticles (red arrow), and the presence of iron is confirmed by Perl's staining (Fig. 3D).

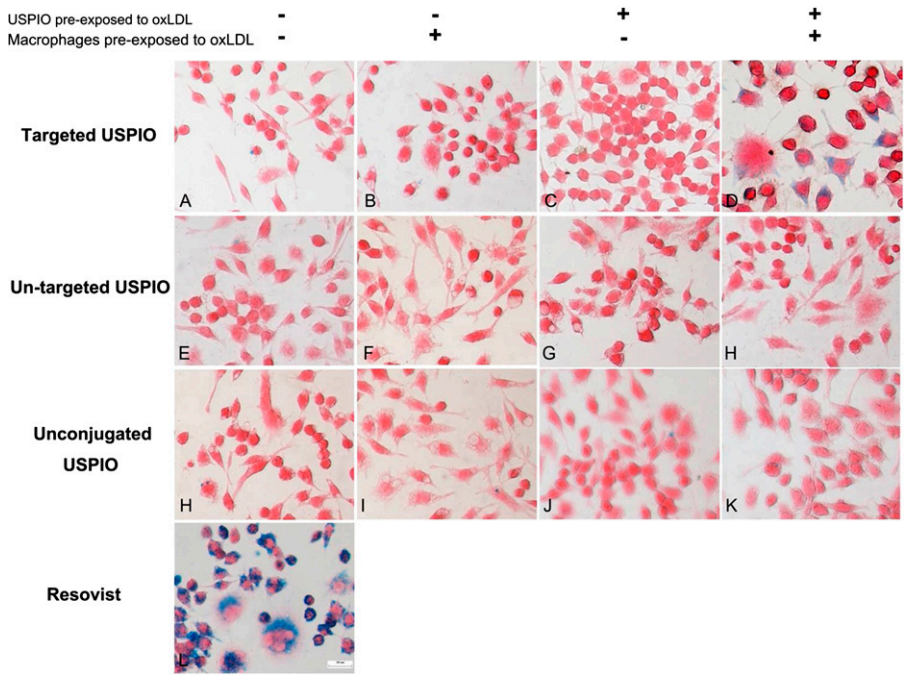

Fig. 2. Macrophages uptake of USPIO nanoparticles. In vitro RAW264.7 macrophages uptake of targeted USPIO, untarget USPIO, and unconjugated USPIO nanoparticles (as negative control) and Resovist (as positive control) with 100 μg Fe/ml for 12 h. Perl's staining for iron oxide uptake was performed. Macrophages were preincubated (+) or not preincubated (−) to mouse OxLDL (100 μg /ml) for 12 h, and iron oxide nanoparticles were preincubated (+) or not preincubated (−) to mouse OxLDL (100 μg /ml) for 2 h before being mixed together in cell culture. Bar = 20 μm.

There were 66 matched image pairs available (24 for anti-OxLDL-USPIO, 16 for untargeted IgG-USPIO, 16 for unconjugated USPIO nanoparticles and 10 for competitive inhibition group, 3–5 image pairs obtained from each mouse) for further comparative analysis. The relative signal intensity changes were −30.4 ± 16% and −34.7 ± 19% for 8 h and 24 h after injection (n = 24). Untargeted IgG-USPIO (Fig. 3E–H) and unconjugated USPIO nanoparticles (Fig. 3I–L) had limited relative signal intensity changes (4.2 ± 17.4% and −4.8 ± 15.8% for untargeted IgG-USPIO nanoparticles [n = 16] and −0.01 ± 27.6% and 1.39 ± 19.0% for unconjugated USPIO nanoparticles [n = 16]). In addition, the simultaneous administration of sufficient free anti-OxLDL antibody with the anti-OxLDL-USPIO nanoparticles significantly inhibited the change in relative signal intensity (−6.9 ± 17.5% and −8.2 ± 16.1%, n = 10, $p < 0.05$) (Fig. 3M–P) (**Fig. 4**). Furthermore, there is a strong correlation between OxLDL/macrophages (CD68+) and positive Perl's staining (**Fig. 5A**, E, I, M; red arrow), confirming the deposition of anti-OxLDL-USPIO nanoparticles in OxLDL enriched

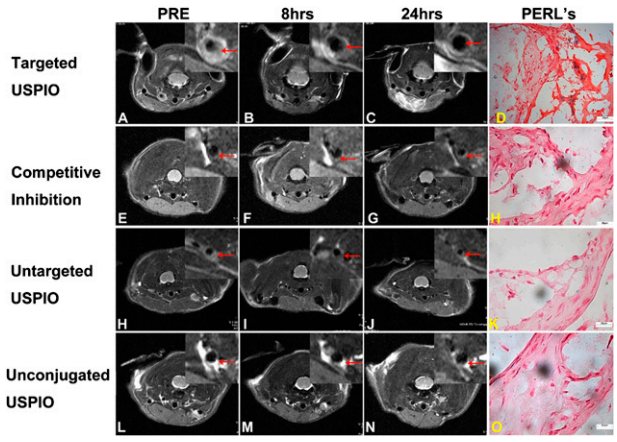

Fig. 3. USPIOs MRI of apoE$^{-/-}$ mice. Representative in vivo carotid atherosclerotic lesion enhancement in apoE$^{-/-}$ mice before and 8 h and 24 h after administration of targeted USPIO, untargeted USPIO, unconjugated USPIO nanoparticles and competitive inhibition (free antibody + anti-OxLDL-USPIO) with a dose of 30 mg Fe/kg body weight. The red arrows indicate the location of signal loss within the plaque. Matched Perl's stained section shows USPIO nanoparticle deposition (blue) within the arterial wall. Bar = 100 μm.

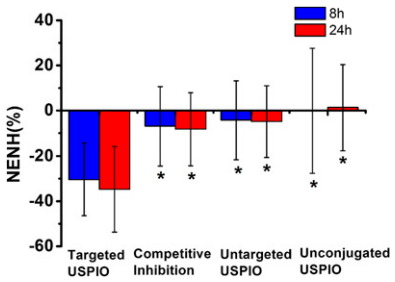

Fig. 4. Relative signal intensity changes among different groups. Comparisons of the relative signal intensity changes (NENH%) in the T_2-weighted images associated with the carotid arterial wall before and after administration of USPIO nanoparticles are shown. * $P < 0.05$ vs. targeted USPIO group.

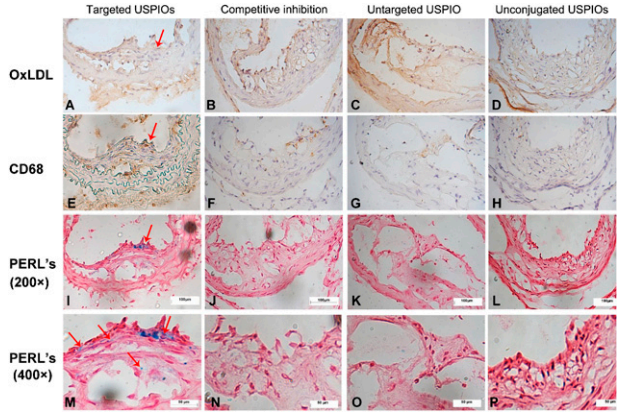

Fig. 5. Immunohistochemistry of carotid lesions of apoE$^{-/-}$ mice. Immunohistochemistry of targeted USPIO, untargeted USPIO, and unconjugated USPIO nanoparticles and competitive inhibition groups in the carotid arterial wall of apoE$^{-/-}$ mice. The carotid arteries wall was stained for OxLDL, macrophage (CD68), and iron oxide (Perl's) deposition (bar = 100 μm). Red arrows indicate the location of iron oxide deposition while OxLDL and macrophages are high expressed in the targeted USPIO group.

macrophages and foam cells. Conversely, even with OxLDL/macrophages (CD68+) present, there is only limited USPIO nanoparticle deposition in atherosclerotic lesions for the competitive inhibition groups (Fig. 5B, F, J, N), the nonspecific IgG-USPIO nanoparticles (Fig. 5C, G, K, O), and unconjugated USPIO nanoparticles (Fig, 5D, H, L, P).

Deposition of anti-OxLDL-USPIO nanoparticles in glomerulus

As in previous studies (34), the PEG-coating does not preclude the final accumulation of USPIO nanoparticles in the reticuloendothelial system because considerable particle uptake was observed in the liver and spleen 24 h after administration (Table 1). However, in an unanticipated finding, histological staining showed a large amount of anti-OxLDL-USPIO nanoparticles deposited in one mouse kidney glomerulus (**Fig. 6A**, red arrow). Furthermore, the presence of macrophages and OxLDL in this glomerulus was confirmed by immunohistochemical staining (Fig. 6B–C, red arrow). In contrast, the other mouse glomeruli in the anti-OxLDL-USPIO group showed limited iron oxide deposition by Perl's staining (Fig. 6D) with corresponding limited staining for OxLDL and CD68 (Fig. 6E–F).

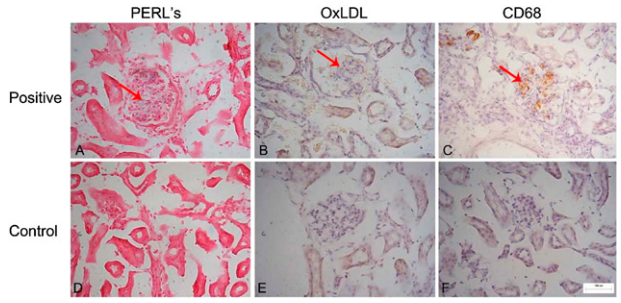

Fig. 6. Immunohistochemistry for glomerulus of apoE$^{-/-}$ mice. Histology and immunohistochemistry for targeted USPIO nanoparticles in kidney glomerulus in apoE$^{-/-}$ mice. The staining is positive for iron oxide deposition (Perl's), OxLDL, and macrophages (CD68) (A–C; red arrow) in kidney glomerulus in apoE$^{-/-}$ mice. The absence of iron oxide deposition in the glomerulus (D) of a control apoE$^{-/-}$ mouse with limited OxLDL and CD68 expression (E, F) is shown. Bar = 100 μm.

DISCUSSION

OxLDL is primarily present in atherosclerotic lesions but not in normal arteries and is associated with increased plaque inflammation and plaque vulnerability. Because of its prominent role in atherosclerosis, OxLDL-targeted molecular imaging has become an area of great research interest (10, 11, 35–38). Although antibodies against different oxidation-specific epitopes have been generated, antibody selection for OxLDL detection is still controversial because of specificity to a single OxLDL epitope (13). To address this challenge, a polyclonal anti-OxLDL antibody may have advantages for detecting OxLDL in vivo due to its ability to bind multiple oxLDL epitopes.

In our preliminary studies, a polyclonal rabbit anti-copper-oxide mouse LDL was produced, and in vitro ELISA assays demonstrated that this polyclonal anti-OxLDL antibody has a high binding specificity to copper-oxide mouse LDL but not to normal mouse LDL. Using this anti-copper-oxide OxLDL antibody, we synthesized a biocompatible, stable, OxLDL-targeted USPIO functioning as an MRI molecular imaging contrast agent in the current study. PEG-coated USPIO using α,ω-dicarboxyl-terminated PEG as a surface capping molecule through a "one-pot reaction" was used (28), which has been well reported to have in vivo tumor detection (25–27). This probe was then used to image carotid atherosclerosis in apoE$^{-/-}$ mice with lesions initiated by bilateral perivascular collar (16). Importantly, we have shown that OxLDL-enriched atherosclerotic lesions can be noninvasively imaged from 8 h to 24 h after anti-OxLDL-USPIO administration. In addition, cotreatment of animals with free anti-OxLDL antibody and anti-OxLDL-USPIO nanoparticles resulted in reduced MR signal changes that may be due to the blocking of available antibody binding sites, similar to Briley-Saebo et al. (12). To our knowledge, this is the first time that OxLDL-targeted USPIO nanoparticles have been used in carotid atherosclerotic lesions of apoE$^{-/-}$ mice. To identify and quantify OxLDL within atherosclerotic lesions, in vivo MRI with targeted probe indicates an important step toward the detection of vulnerable plaques (8, 10).

Sinerem (Ferumoxtran-10; Guerbet, Roissy, France), a commercial dextran-coated USPIO nanoparticle, has been used in clinical studies to identify carotid plaque inflammation (31, 39) and to assess therapeutic response to atorvastatin therapy (21). These dextran-coated iron oxide particles are passively taken up by a variety of activated macrophages within the artery wall and are best imaged 24–36 h after administration. On the other hand, PEG-coated iron oxides, as presented in the current work, are known to reduce plasma protein binding, delay clearance

by the reticuloendothelial system, and increase particle circulation times (25, 26, 29). These factors increase the probability of the targeted iron oxide nanoparticles reaching the tissue of interest (28). Our in vitro experiments confirmed that the PEG-coated USPIOs are not passively taken up by macrophages or foam cells (macrophages exposed to OxLDL for 12 h), except when they are conjugated to anti-OxLDL antibody and after binding free OxLDL (Fig. 2D) (8, 10). Briley-Saebo et al. (8) demonstrated that OSE-targeted, PEG-coated nanoparticles (lipid-coated SPIO or lipid-coated USPIO nanoparticles) may bind extracellular OxLDL or OxLDL bound to macrophage scavenger receptors and selectively accumulate within lipid-rich J774A.1 macrophages and foam cells. Our in vitro data show similar results in RAW264.7 macrophages. Future studies are warranted to evaluate the immune response to the polyclonal antibodies and the mechanism of uptake for targeted PEG-coated USPIO by macrophages.

Targeted anti-OxLDL-USPIO nanoparticles exhibited a significantly longer circulating half-life than the untargeted IgG-USPIO. However, this was noted only in apoE$^{-/-}$ mice, which may have higher levels of circulating OxLDL in the blood and vessel wall, similar to the previous studies (8). It is expected that the binding of targeted anti-OxLDL-USPIO nanoparticles to circulating OxLDL may have reduced blood clearance (8, 35). For imaging, the increased blood half-life of the targeted nanoparticles was likely beneficial because it allows greater time for accumulation of the particles within the arterial wall and greater uptake by macrophages.

In a related study, Briley-Saebo et al. (8) used MDA2, E06, and IK17 PEG-linked to the surface of lipid coated USPIO nanoparticles to construct iron oxide probes targeted to OSE and imaged the nanoparticles in an apoE$^{-/-}$ mouse aorta atherosclerotic plaque model. The MRI results showed significant signal loss 24 h after administration of all the oxidation-specific epitope targeted LUSPIO formulations (MDA2-LUSPIO, E06-LUSPIO, and IK17-LUSPIO) in apoE$^{-/-}$ mice and was confirmed by gradient echo acquisition for superparamagnetic particles with positive contrast images and histology. In addition, MDA2, E06, and IK17 linked to the surface of micelles containing gadolinium (10) or MDA2, E06, and IK17 linked to the surface of micelles containing manganese (9) have been used to detect OSE in aortic atherosclerotic lesions in apoE$^{-/-}$ mice and LDLR$^{-/-}$ mice. However, monoantibodies, such as MDA2, E06, and IK17, can only detect single oxidation-specific epitopes in atherosclerotic lesions. Furthermore, these antibodies were not available for most laboratories. Finally, the animal models used in the study by Briley-Saebo et al. study have several disadvantages. Although the aortic atherosclerotic lesions are relatively straightforward to locate for histological processing, thereby making it easy to standardize across experiments and laboratories, it does not exhibit intraplaque hemorrhage or any other sign of plaque disruption in apoE$^{-/-}$ mice or LDLR$^{-/-}$ mice, even after extended periods of fat feeding (14). The use of aortic atherosclerotic lesions for investigations of plaque rupture is still controversial (15, 40).

In comparison, the perivascular collar model used in current study offers the advantage of maintaining the structural integrity of the endothelium while inducing rapid, site-controlled atherosclerotic lesions formation (16). First, carotid plaques induced by perivascular collar develop much faster than those of other models. Rapid atherogenesis allows efficient screening of potentially anti-atherogenic new chemical entities and the valuation of therapies with a limited duration of effectiveness. Second, lesions in this perivascular collar model develop immediately proximal to the collar, elicited by low wall shear stress in this region, and are strictly dependent on the presence of hypercholesterolemia, which the two key etiologic factors are known to drive spontaneous human atherosclerosis. Third, the carotid artery of apoE$^{-/-}$ mice is easily accessible and can be repeatedly exposed for gene or pharmacological interventions (16, 41, 42).

The current studies using polyclonal anti-OxLDL antibody conjugated USPIO nanoparticles targeted to OxLDL in vivo show significant signal loss in carotid atherosclerotic lesions at 8 h after administration that remains at 24 h in T2-weighted MR images. Immunohistochemistry confirmed the colocalization of the OxLDL/macrophages and iron oxide nanoparticles. Moreover, the simultaneous administration of sufficient free anti-OxLDL antibody with the anti-OxLDL-USPIO nanoparticles significantly inhibited the change in relative signal intensity. These results indicate that a polyclonal anti-OxLDL antibody can be used for the molecular imaging of OxLDL in vivo with sensitivity similar to monoclonal antibodies or fragments and validate that noninvasive imaging of OxLDL within the atherosclerotic lesions is possible by using OxLDL-targeted nanoparticles. If translated to clinical applications, this approach may provide a valuable tool for noninvasively detecting, quantifying, and monitoring vulnerable atherosclerotic plaques.

An unexpected finding was the deposition of anti-OxLDL-USPIO nanoparticles in the kidney glomerulus of one apoE$^{-/-}$ mouse, which was colocalized with OxLDL and CD68(+) macrophages. First, this proves that anti-OxLDL-USPIO nanoparticles target OxLDL beyond carotid atherosclerotic plaque lesions. This potential is encouraging because OxLDL and oxidative stress play key roles in the development of glomerular disease. Second, it provides further evidence of the specificity of anti-OxLDL-USPIO nanoparticles to OxLDL and macrophages, especially OxLDL-enriched and activated macrophages.

Limitations of the current study include the fact that we can only hypothesize as to the mechanism of targeted-USPIO nanoparticle uptake and the degree of immune response to the polyclonal antibodies. These questions require multistaged future investigations. Another limitation of our in vivo approach was the large USPIO dose compared with clinical studies (30 mg iron/kg vs. 5.6 mg iron/kg body weight), although no clinical signs of toxicity were observed during or after iron oxide administration. One challenge is that neovascularization in carotid

atherosclerotic lesions is far less than in aortic atherosclerotic lesions in apoE$^{-/-}$ mice (43), and neovascularization in the neointima plays a pivotal role for USPIO nanoparticle deposition into plaque. Another challenge is that USPIOs less than 25 nm in diameter may diffuse in the plaques more easily because the aorta endothelial tight gap junction associated with the plaque is approximately 20 nm in apoE$^{-/-}$ mice (8). Advancements in the "one-pot" reaction process have led to a new kind of biocompatible Fe_3O_4 nanocrystal with a smaller mean size (6.6 ± 1.1 nm) that is now commercially available (http://www.oneder-hightech.com). We anticipate that future studies using this smaller-sized USPIO nanoparticles could reduce the USPIO dose.

In conclusion, the present study demonstrates a novel method for noninvasively imaging an important mediator of cardiovascular disease, OxLDL, within carotid atherosclerotic lesions. Additionally, these OxLDL-targeted USPIO nanoparticles may have the potential to noninvasively image glomerular disease. Continuing studies are warranted to confirm these encouraging results.

The authors thank Dr. Rui Li and Dr. Xihai Zhao at the Center for Biomedical Imaging Research, Tsinghua University, Beijing, China for assistance in magnetic relaxation analysis and Dr. Min Yang at Jiangsu Institute of Nuclear Medicine, Dr. Chenglong Yan, and Dr. Yan Wang at Wuxi Molecular imaging CRO center for their excellent help with the nanoparticles ^{125}I-labeling, pharmacokinetics, and bio-distribution experiments.

REFERENCES

1. Roger, V. L., A. S. Go, D. M. Lloyd-Jones, R. J. Adams, J. D. Berry, T. M. Brown, M. R. Carnethon, S. Dai, G. de Simone, E. S. Ford, et al. 2011. Heart disease and stroke statistics–2011 update: a report from the American Heart Association. *Circulation.* **123:** e18–e209.
2. Fuster, V., P. R. Moreno, Z. A. Fayad, R. Corti, and J. J. Badimon. 2005. Atherothrombosis and high-risk plaque: part I: evolving concepts. *J. Am. Coll. Cardiol.* **46:** 937–954.
3. Fayad, Z. A. 2001. The assessment of the vulnerable atherosclerotic plaque using MR imaging: a brief review. *Int. J. Cardiovasc. Imaging.* **17:** 165–177.
4. Matsuura, E., G. R. Hughes, and M. A. Khamashta. 2008. Oxidation of LDL and its clinical implication. *Autoimmun. Rev.* **7:** 558–566.
5. Namgaladze, D., A. Kollas, and B. Brune. 2008. Oxidized LDL attenuates apoptosis in monocytic cells by activating ERK signaling. *J. Lipid Res.* **49:** 58–65.
6. Nishi, K., H. Itabe, M. Uno, K. T. Kitazato, H. Horiguchi, K. Shinno, and S. Nagahiro. 2002. Oxidized LDL in carotid plaques and plasma associates with plaque instability. *Arterioscler. Thromb. Vasc. Biol.* **22:** 1649–1654.
7. Ishigaki, Y., H. Katagiri, J. Gao, T. Yamada, J. Imai, K. Uno, Y. Hasegawa, K. Kaneko, T. Ogihara, H. Ishihara, et al. 2008. Impact of plasma oxidized low-density lipoprotein removal on atherosclerosis. *Circulation.* **118:** 75–83.
8. Briley-Saebo, K. C., Y. S. Cho, P. X. Shaw, S. K. Ryu, V. Mani, S. Dickson, E. Izadmehr, S. Green, Z. A. Fayad, and S. Tsimikas. 2011. Targeted iron oxide particles for in vivo magnetic resonance detection of atherosclerotic lesions with antibodies directed to oxidation-specific epitopes. *J. Am. Coll. Cardiol.* **57:** 337–347.
9. Briley-Saebo, K. C., T. H. Nguyen, A. M. Saeboe, Y. S. Cho, S. K. Ryu, E. Volkava, S. Dickson, G. Leibundgut, P. Weisner, S. Green, et al. 2012. In vivo detection of oxidation-specific epitopes in atherosclerotic lesions using biocompatible manganese molecular magnetic imaging probes. *J. Am. Coll. Cardiol.* **59:** 616–626.
10. Briley-Saebo, K. C., P. X. Shaw, W. J. Mulder, S. H. Choi, E. Vucic, J. G. Aguinaldo, J. L. Witztum, V. Fuster, S. Tsimikas, and Z. A. Fayad. 2008. Targeted molecular probes for imaging atherosclerotic lesions with magnetic resonance using antibodies that recognize oxidation-specific epitopes. *Circulation.* **117:** 3206–3215.
11. Briley-Saebo, K. C., Y. S. Cho, and S. Tsimikas. 2011. Imaging of oxidation-specific epitopes in atherosclerosis and macrophage-rich vulnerable plaques. *Curr Cardiovasc Imaging Rep.* **4:** 4–16.
12. Wu, T., W. C. Willett, N. Rifai, I. Shai, J. E. Manson, and E. B. Rimm. 2006. Is plasma oxidized low-density lipoprotein, measured with the widely used antibody 4E6, an independent predictor of coronary heart disease among US men and women? *J. Am. Coll. Cardiol.* **48:** 973–979.
13. Ishigaki, Y., Y. Oka, and H. Katagiri. 2009. Circulating oxidized LDL: a biomarker and a pathogenic factor. *Curr. Opin. Lipidol.* **20:** 363–369.
14. Jackson, C. L., M. R. Bennett, E. A. Biessen, J. L. Johnson, and R. Krams. 2007. Assessment of unstable atherosclerosis in mice. *Arterioscler. Thromb. Vasc. Biol.* **27:** 714–720.
15. Majesky, M. W. 2002. Mouse model for atherosclerotic plaque rupture. *Circulation.* **105:** 2010–2011.
16. von der Thusen, J. H., T. J. van Berkel, and E. A. Biessen. 2001. Induction of rapid atherogenesis by perivascular carotid collar placement in apolipoprotein E-deficient and low-density lipoprotein receptor-deficient mice. *Circulation.* **103:** 1164–1170.
17. Chyu, K. Y., S. M. Babbidge, X. Zhao, R. Dandillaya, A. G. Rietveld, J. Yano, P. Dimayuga, B. Cercek, and P. K. Shah. 2004. Differential effects of green tea-derived catechin on developing versus established atherosclerosis in apolipoprotein E-null mice. *Circulation.* **109:** 2448–2453.
18. Yuan, C., L. M. Mitsumori, M. S. Ferguson, N. L. Polissar, D. Echelard, G. Ortiz, R. Small, J. W. Davies, W. S. Kerwin, and T. S. Hatsukami. 2001. In vivo accuracy of multispectral magnetic resonance imaging for identifying lipid-rich necrotic cores and intraplaque hemorrhage in advanced human carotid plaques. *Circulation.* **104:** 2051–2056.
19. Saam, T., T. S. Hatsukami, N. Takaya, B. Chu, H. Underhill, W. S. Kerwin, J. Cai, M. S. Ferguson, and C. Yuan. 2007. The vulnerable, or high-risk, atherosclerotic plaque: noninvasive MR imaging for characterization and assessment. *Radiology.* **244:** 64–77.
20. Wang, J., N. Balu, G. Canton, and C. Yuan. 2010. Imaging biomarkers of cardiovascular disease. *J. Magn. Reson. Imaging.* **32:** 502–515.
21. Tang, T. Y., S. P. Howarth, S. R. Miller, M. J. Graves, A. J. Patterson, J. M. U-King-Im, Z. Y. Li, S. R. Walsh, A. P. Brown, P. J. Kirkpatrick, E. A. Warburton, P. D. Hayes, K. Varty, J. R. Boyle, M. E. Gaunt, A. Zalewski, and J. H. Gillard. 2009. The ATHEROMA (Atorvastatin Therapy: Effects on Reduction of Macrophage Activity) study. Evaluation using ultrasmall superparamagnetic iron oxide-enhanced magnetic resonance imaging in carotid disease. *J. Am. Coll. Cardiol.* **53:** 2039–2050.
22. Persigehl, T., R. Bieker, L. Matuszewski, A. Wall, T. Kessler, H. Kooijman, N. Meier, W. Ebert, W. E. Berdel, W. Heindel, et al. 2007. Antiangiogenic tumor treatment: early noninvasive monitoring with USPIO-enhanced MR imaging in mice. *Radiology.* **244:** 449–456.
23. Winter, P. M., A. M. Morawski, S. D. Caruthers, R. W. Fuhrhop, H. Zhang, T. A. Williams, J. S. Allen, E. K. Lacy, J. D. Robertson, G. M. Lanza, et al. 2003. Molecular imaging of angiogenesis in early-stage atherosclerosis with alpha(v)beta3-integrin-targeted nanoparticles. *Circulation.* **108:** 2270–2274.
24. Trivedi, R. A., J. M. U-King-Im, M. J. Graves, J. J. Cross, J. Horsley, M. J. Goddard, J. N. Skepper, G. Quartey, E. Warburton, I. Joubert, L. Wang, P. J. Kirkpatrick, J. Brown, and J. H. Gillard. 2004. In vivo detection of macrophages in human carotid atheroma: temporal dependence of ultrasmall superparamagnetic particles of iron oxide-enhanced MRI. *Stroke.* **35:** 1631–1635.
25. Zhen, L., L. Wei, M. Y. Gao, and H. Lei. 2005. One-pot reaction to synthesize biocompatible magnetite nanoparticles. *Adv. Mater. (Deerfield Beach Fla.).* **17:** 1001–1005.
26. Hu, F. Q., W. Li, Z. Zhou, Y. L. Ran, L. Zhen, and M. Y. Gao. 2006. Preparation of biocompatible magnetite nanocrystals for in vivo magnetic resonance detection of cancer. *Adv. Mater. (Deerfield Beach Fla.).* **18:** 2553–2556.
27. Liu, S. J., B. Jia, R. R. Qiao, Z. Yang, Z. L. Yu, Z. F. Liu, K. Liu, J. Y. Shi, H. Ouyang, F. Wang, et al. 2009. A novel type of dual-modality molecular probe for mr and nuclear imaging of tumor:

preparation, characterization and in vivo application. *Mol. Pharm.* **6:** 1074–1082.
28. Gao, Q., J. Zhang, G. Hong, and J. Ni. 2010. One-pot reaction to synthesize PEG-coated hollow magnetite nanostructures with excellent magnetic properties. *J. Nanosci. Nanotechnol.* **10:** 6400–6406.
29. Liu, D. F., W. Wu, J. J. Ling, S. Wen, N. Gu, and X. Z. Zhang. 2011. Effective PEGylation of iron oxide nanoparticles for high performance in vivo cancer imaging. *Adv. Funct. Mater.* **21:** 1498–1504.
30. Denny, J. B., and G. Blobel. 1984. 125I-labeled crosslinking reagent that is hydrophilic, photoactivatable, and cleavable through an azo linkage. *Proc. Natl. Acad. Sci. USA.* **81:** 5286–5290.
31. Trivedi, R. A., C. Mallawarachi, J. M. U-King-Im, M. J. Graves, J. Horsley, M. J. Goddard, A. Brown, L. Wang, P. J. Kirkpatrick, J. Brown, and J. H. Gillard. 2006. Identifying inflamed carotid plaques using in vivo USPIO-enhanced MR imaging to label plaque macrophages. *Arterioscler. Thromb. Vasc. Biol.* **26:** 1601–1606.
32. Shen, T., R. Weissleder, M. Papisov, A. Bogdanov, Jr., and T. J. Brady. 1993. Monocrystalline iron oxide nanocompounds (MION): physicochemical properties. *Magn. Reson. Med.* **29:** 599–604.
33. Wunderbaldinger, P., L. Josephson, and R. Weissleder. 2002. Tat peptide directs enhanced clearance and hepatic permeability of magnetic nanoparticles. *Bioconjug. Chem.* **13:** 264–268.
34. Radermacher, K. A., N. Beghein, S. Boutry, S. Laurent, L. Vander Elst, R. N. Muller, B. F. Jordan, and B. Gallez. 2009. In vivo detection of inflammation using pegylated iron oxide particles targeted at E-selectin: a multimodal approach using MR imaging and EPR spectroscopy. *Invest. Radiol.* **44:** 398–404.
35. Briley-Saebo, K. C., W. J. Mulder, V. Mani, F. Hyafil, V. Amirbekian, J. G. Aguinaldo, E. A. Fisher, and Z. A. Fayad. 2007. Magnetic resonance imaging of vulnerable atherosclerotic plaques: current imaging strategies and molecular imaging probes. *J. Magn. Reson. Imaging.* **26:** 460–479.
36. Tsimikas, S., B. P. Shortal, J. L. Witztum, and W. Palinski. 2000. In vivo uptake of radiolabeled MDA2, an oxidation-specific monoclonal antibody, provides an accurate measure of atherosclerotic lesions rich in oxidized LDL and is highly sensitive to their regression. *Arterioscler. Thromb. Vasc. Biol.* **20:** 689–697.
37. Torzewski, M., P. X. Shaw, K. R. Han, B. Shortal, K. J. Lackner, J. L. Witztum, W. Palinski, and S. Tsimikas. 2004. Reduced in vivo aortic uptake of radiolabeled oxidation-specific antibodies reflects changes in plaque composition consistent with plaque stabilization. *Arterioscler. Thromb. Vasc. Biol.* **24:** 2307–2312.
38. Tsimikas, S. 2002. Noninvasive imaging of oxidized low-density lipoprotein in atherosclerotic plaques with tagged oxidation-specific antibodies. *Am. J. Cardiol.* **90:** 22L–27L.
39. Tang, T. Y., S. P. Howarth, S. R. Miller, M. J. Graves, J. M. U-King-Im, Z. Y. Li, S. R. Walsh, A. J. Patterson, P. J. Kirkpatrick, E. A. Warburton, K. Varty, M. E. Gaunt, and J. H. Gillard. 2008. Correlation of carotid atheromatous plaque inflammation using USPIO-enhanced MR imaging with degree of luminal stenosis. *Stroke.* **39:** 2144–2147.
40. Falk, E., S. M. Schwartz, Z. S. Galis, and M. E. Rosenfeld. 2007. Putative murine models of plaque rupture. *Arterioscler. Thromb. Vasc. Biol.* **27:** 969–972.
41. von der Thusen, J. H., B. J. van Vlijmen, R. C. Hoeben, M. M. Kockx, L. M. Havekes, T. J. van Berkel, and E. A. Biessen. 2002. Induction of atherosclerotic plaque rupture in apolipoprotein E−/− mice after adenovirus-mediated transfer of p53. *Circulation.* **105:** 2064–2070.
42. Ni, M., Y. Wang, M. Zhang, P. F. Zhang, S. F. Ding, C. X. Liu, X. L. Liu, Y. X. Zhao, and Y. Zhang. 2009. Atherosclerotic plaque disruption induced by stress and lipopolysaccharide in apolipoprotein E knockout mice. *Am. J. Physiol. Heart Circ. Physiol.* **296:** H1598–H1606.
43. Johnson, J., K. Carson, H. Williams, S. Karanam, A. Newby, G. Angelini, S. George, and C. Jackson. 2005. Plaque rupture after short periods of fat feeding in the apolipoprotein E-knockout mouse: model characterization and effects of pravastatin treatment. *Circulation.* **111:** 1422–1430.